Article

Not peer-reviewed version

Analysis of Vertical-Axis Wind-Turbine Clusters Using Condensed Two-Dimensional Velocity Data Obtained from Three-Dimensional Computational Fluid Dynamics

Md. Shameem Moral * , Hiroto Inai , Yutaka Hara * , Yoshifumi Jodai , Hongzhong Zhu

Posted Date: 31 March 2026

doi: 10.20944/preprints202603.0019.v2

Keywords: wind energy; vertical-axis wind turbine; fast computation; condensed velocity data; wind farm; turbine-cluster; gap dependence

Preprints.org (www.preprints.org) | NOT PEER-REVIEWED | Posted: 31 March 2026 doi:10.20944/preprints202603.0019.v2

Article

Analysis of Vertical-Axis Wind-Turbine Clusters Using Condensed Two-Dimensional Velocity Data Obtained from Three-Dimensional Computational Fluid Dynamics

Md. Shameem Moral [1,*], Hiroto Inai [1], Yutaka Hara [2,*], Yoshifumi Jodai [3] and Hongzhong Zhu [4]

[1] Graduate School of Engineering, Tottori University, 4-101 Koyama-Minami, Tottori 680-8552, Japan
[2] Advanced Mechanical and Electronic System Research Center (AMES), Faculty of Engineering, Tottori University, 4-101 Koyama-Minami, Tottori 680-8552, Japan
[3] Department of Mechanical Engineering, National Institute of Technology (KOSEN), Kagawa College, 355 Chokushi, Takamatsu 761-8058, Japan
[4] Research Institute for Applied Mechanics, Kyushu University, 6-1 Kasuga-Koen, Kasuga, Fukuoka 816-8580, Japan
* Correspondence: tottoriuni202310@gmail.com (M.S.M.); hara@tottori-u.ac.jp (Y.H.);
Tel.: +81-70-7562-2662 (M.S.M.); +81-857-31-6758 (Y.H.)

Abstract

Vertical-axis wind turbine (VAWT) clusters have been extensively investigated owing to their positive aerodynamic interactions. However, accurate predictions of the flow field and power output of each rotor in VAWT clusters using high-fidelity computational fluid dynamics (CFD) remain computationally expensive. In this study, we propose a fast computation method for the flow field and operating state of each rotor of VAWT clusters using temporally and spatially averaged velocity data compressed from an unsteady velocity field obtained via a 3D-CFD simulation of an isolated single rotor. First, the unsteady 3D flow field in the 3D-CFD simulation is time-averaged over several revolutions. Next, the temporally averaged velocity is spatially averaged in the vertical direction to obtain spatially compressed data. Based on a previously developed fast computation framework, a wind-farm flow field is constructed using condensed two-dimensional velocity data obtained from a single turbine. The proposed method is applied to three-rotor configurations, and the rotational speeds of the turbines are compared with the wind-tunnel measurements. The results show that the proposed method substantially improved the prediction accuracy while maintaining a low computational cost. In addition, it can be used to efficiently design and optimize turbine layouts in VAWT wind farms.

Keywords: wind energy; vertical-axis wind turbine; fast computation; condensed velocity data; wind farm; turbine-cluster; gap dependence

1. Introduction

The realization of a decarbonized society requires the rapid and large-scale deployment of renewable energy technologies. Among various renewable energy sources, wind energy is particularly important because of its technological maturity, low cost, and applicability to both onshore and offshore installations [1,2]. Currently, large horizontal-axis wind turbines (HAWTs) dominate the commercial wind-energy market owing to their high power-conversion efficiency and well-established design methodologies. However, the installation of large HAWTs typically excludes urban or geographically constrained regions because of land availability, visual impact, noise concerns, and complex infrastructure requirements [3,4].

doi:10.20944/preprints202603.0019.v2

By contrast, vertical-axis wind turbines (VAWTs), particularly small-scale VAWTs, are expected to serve as distributed power-generation systems. Small VAWTs possess several inherent advantages over HAWTs, including insensitivity to the wind direction in terms of power generation (for a single turbine), simplified mechanical structure, reduced noise emissions, and ease of installation and maintenance [5]. These characteristics render small VAWTs suitable for urban environments, regions where large equipment cannot be easily transported, and locations with highly variable wind directions. However, when operated as standalone turbines, small VAWTs incur relatively high costs per unit power output, limiting their widespread adoption. To promote the deployment of VAWTs, researchers have recently focused on closely spaced VAWT clusters, which feature multiple turbines arranged in compact configurations [6–10]. Unlike HAWT wind farms, which require large inter-turbine spacing to mitigate wake losses, VAWTs can be placed much closer together. Several studies have demonstrated that, under certain configurations, aerodynamic interactions between neighboring VAWTs yield constructive wake effects, thereby increasing the power output per turbine and power density per unit land area [11].

Despite these promising findings, accurately predicting aerodynamic interactions within VAWT clusters remains a significant challenge. The flow field around a VAWT is inherently unsteady, three-dimensional (3D), and accompanied by complex wake structures caused by dynamic stalls, blade–vortex interactions, and related phenomena [12,13]. High-fidelity computational fluid dynamics (CFD) simulations [14] can accurately capture these effects. However, the computational cost increases with the number of turbines, rendering full three-dimensional computational fluid dynamics (3D-CFD) simulations impractical for the flow-field analysis and layout optimization of large VAWT wind farms [10].

Hence, researchers have applied wake models originally developed for HAWTs to optimize turbine placement in VAWT wind farms [15–17]. Although these approaches may be effective when turbines are sufficiently separated, they are based on fundamentally different wake characteristics and are thus likely to exhibit reduced accuracy when the VAWTs are closely spaced.

Several approaches have been proposed to reduce the computational cost of CFD analyses of VAWTs, including reduced-order modeling, parameterization, and surrogate modeling. Bangga et al. [18] conducted a comprehensive assessment of three VAWTs with different solidities using three CFD codes, engineering models based on the blade element momentum (BEM) theory (including modified versions accounting for streamtube expansion and unsteady effects), and the vortex method, and discussed the characteristics and limitations of each approach. Brusca et al. [19] developed a fast computational method capable of deriving performance curves from only three CFD simulations of a ducted Savonius wind turbine aimed at power augmentation. Chen et al. [20] addressed the problem of predicting the mean torque of each rotor at the optimal tip-speed ratio for twin VAWTs arranged obliquely to the main flow, using the pitch angle combinations of the upstream and downstream rotors as inputs. They applied two surrogate models, namely a Kriging model [21] and an artificial neural network (ANN) [22], and compared their performance. Both models provided rapid and accurate predictions using a limited number of CFD results as training data.

Hara et al. [23] proposed a fast computation method for the flow field and power output of each rotor in VAWT wind farms by efficiently representing turbine interactions through the superposition of two-dimensional computational fluid dynamics (2D-CFD) data of a single VAWT rotor. Subsequently, Moral et al. demonstrated that the results of this approach are independent of the order in which the turbines are computed, and thus proposed an improved fast computation method (method-2 in [24] is called the improved fast computation method (IFCM) in this study). However, when the IFCM was applied to predict the rotational speeds of a realistic 3D miniature turbine cluster (three turbines in parallel) tested in a wind tunnel, the predictions underestimated the experimental results for short rotor spacings, even when the single-turbine flow data used as the basis of the flow reconstruction were replaced with the velocity distributions measured at the equatorial plane using a hot-wire anemometer [25]. In this case, the relative trends in the rotational speeds of the three turbines differed from those in the experiments. In contrast, when 2D-CFD data were used, the rotational speeds were overestimated for short spacings, although the relative ordering of the turbine rotational speeds was similar to the experimental observations. These results indicate the necessity of incorporating 3D-CFD information.

Accordingly, the present study performs unsteady 3D-CFD simulations of the flow field around a single miniature turbine (diameter D = 50 mm) used in previous wind-tunnel experiments [26] to obtain time-averaged flow fields. Based on the resulting 3D steady velocity field, the vertical averages of the horizontal velocity components were computed within a layered volume encompassing the rotor height to construct a condensed two-dimensional (2D) velocity field. The objective of this study is to demonstrate that using this compressed 2D dataset as input to the previously developed in-house software, VAWTWF, based on IFCM, improves the prediction accuracy for realistic VAWT clusters. The predicted rotational speeds are compared with wind-tunnel measurements obtained for three types of closely spaced miniature turbine configurations: three turbines in parallel [27], three turbines in tandem [28], and an equilateral triangular arrangement [29].

The novelty of this study lies in the use of 2D velocity data obtained by compressing the 3D-CFD results of a single isolated wind turbine as an input for a fast computational method for VAWT wind farms. By retaining the essential information of the 3D flow field, the proposed method enables both improved computational accuracy and a substantial reduction in the computational cost for the analysis of VAWT wind farms.

The remainder of this paper is organized as follows: Section 2.1 describes the 3D-CFD analysis of a miniature turbine and the procedure for generating a condensed 2D velocity field. Section 2.2 presents the characteristics of the target turbine and their relationship with the applied load torque. Section 2.3 outlines the fast computational method for simulating the flow field, power output, and rotational speed of VAWT wind farms. Section 3 presents the application of the method to three types of VAWT clusters comprising three miniature turbines for which wind-tunnel data are available. Sections 3.1, 3.2, and 3.3 present analyses of the parallel, tandem, and equilateral triangular configurations, respectively, with comparisons and discussions of the predicted and measured rotational speeds of each turbine. Finally, Section 4 summarizes the conclusions of the study.

2. Materials and Methods

2.1. 3D-CFD of Miniature Turbine and Construction of Condensed 2D Velocity Field

In this study, CFD simulations were performed using STAR-CCM+ (Siemens, version 2520) for a miniature butterfly-type VAWT. Figure 1a shows the 3D model of the target turbine. The turbine dimensions are identical to those of the model used in the wind-tunnel experiments conducted at the National Institute of Technology, Kagawa College [30]: rotor height H = 43.4 mm, rotor diameter D = 50 mm, and hub diameter D_{hub} = 18 mm. The blade chord length at the equatorial section is c = 20 mm, the airfoil is NACA 0018, and the number of blades is B = 3.

The governing equations are the incompressible continuity and Reynolds-averaged Navier–Stokes equations, and an unsteady 3D analysis was performed. A segregated-flow solver was used. Temporal advancement was performed using an implicit scheme, and second-order temporal discretization was adopted. Turbulence effects were modeled using the shear stress transport k-ω turbulence model [31]. As shown in Figure 1b, the entire computational domain (stationary region 1) was defined as a rectangular parallelepiped measuring 40D (2000 mm) in the streamwise direction, 50D (2500 mm) in the lateral direction, and 20D (1000 mm) in height. Trimmed meshes were used throughout the domain except in the vicinity of the rotor surface. The turbine was positioned such that its center was located 20D (1000 mm) downstream of the inlet boundary. The upstream boundary of stationary region 1 was specified as a velocity inlet with a uniform inflow velocity U_∞ = 10 m/s. The outlet boundary was defined as the pressure outlet with a gauge pressure of 0.0 Pa. The lateral boundaries were assigned slip conditions, and the turbine surface was modeled as a no-slip wall. As illustrated in Figure 1c, the turbine model was placed inside a cylindrical rotating region with a diameter of 1.4D (70 mm) and a height of 1.6H (70 mm), surrounded by an overlapping mesh-control region (diameter $1.6D$ (80 mm), height $1.8H$ (80 mm)). To comprehensively capture the flow field around the turbine, a rectangular parallelepiped stationary region 2 enclosing the turbine was defined, in which a uniformly fine mesh was adopted. This region spanned $5D$ (250 mm) in the lateral direction, $2D$ (100 mm) upstream, $6D$ (300 mm) downstream from the turbine center, and $4D$ (200 mm) in the vertical direction. As shown in Figure 1d, prism-layer meshes with a layered configuration were applied near the blade surfaces. The prism-layer, which featured 10 layers and a growth rate of 1.5, measured 0.33 mm thick, and the near-wall resolution was set such that the nondimensional wall distance $y^+ < 1$. The mesh on the rotor surface is shown in Figure 1a. The rotating region containing the rotor and surrounding stationary region 2 were connected using an overset-mesh technique. The grid contained approximately 12 million cells in stationary region 1 (including stationary region 2) and approximately 4 million cells in the rotating region, resulting in approximately 16 million cells in the entire computational domain.

To examine the mesh dependency of the present 3D-CFD simulations, additional computations were conducted with a finer mesh of approximately 20 million cells and a coarser mesh of approximately 6 million cells, compared with the current 16 million-cell mesh. The mean power coefficients, C_P, obtained by averaging over the fifth revolution were 0.092566, 0.093290, and 0.106139 for the coarse, medium, and fine meshes, respectively. Taking the 20 million-cell mesh as the reference, the 6 million-cell mesh underestimates C_P by 12.79%, whereas the 16 million-cell mesh underestimates C_P by 12.11%. Given the computational cost of time averaging, a 16-million-cell mesh was adopted in this study.

Based on previous experimental results at a wind speed of 10 m/s, the turbine was rotated at a constant speed of $N = 2612$ rpm. The direction of rotation was counterclockwise when viewed from above. The time step was 3.19×10^{-5} s, which corresponded to a rotor rotation of 0.5° per time step. The simulation was conducted until the turbine completed 15 revolutions, at which point the time-averaged velocity distribution almost converged. For the computations after the second rotation, the Courant number was maintained below 100. In the present CFD simulation based on an implicit scheme, the Courant number was within an acceptable range. The Reynolds number, based on the rotor diameter and freestream velocity, was 3.3×10^4.

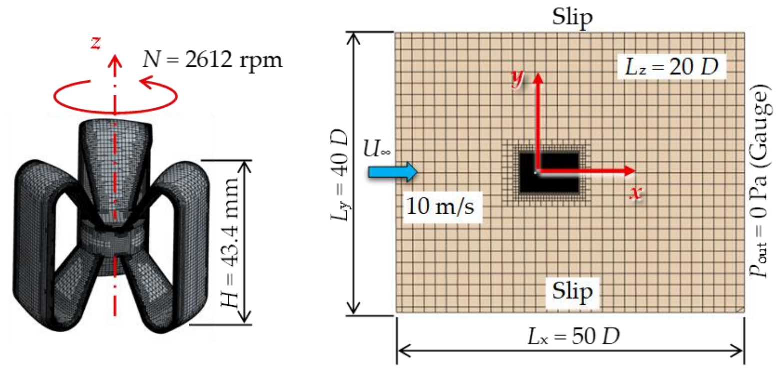

(**a**) Wind turbine part (**b**) Entire computational domain

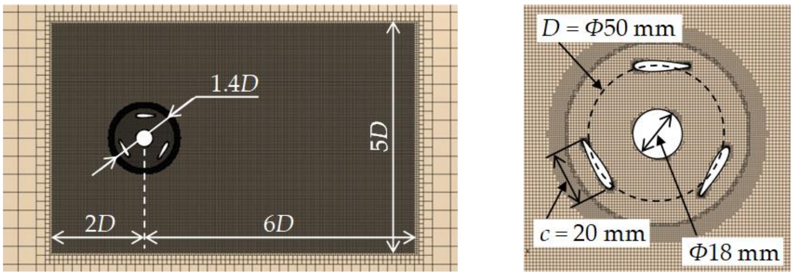

(**c**) Near-wake region (**d**) Near-rotor region

Figure 1. Computational grids created for 3D-CFD of single miniature VAWT.

Figure 2a shows the unsteady vortex shedding using an isosurface of the *Q*-criterion ($Q = 10^5\ \mathrm{s}^{-2}$) [32], where the color indicates the vorticity magnitude on the isosurface. Figure 2b shows the instantaneous distribution of the streamwise velocity component u on the equatorial plane. Because almost periodic vortex shedding was observed within the first five revolutions after the computation commenced, the velocity components (u, v, and w) were time-averaged over the subsequent 10 revolutions (from the 6th to 15th revolutions) to obtain the 3D mean flow fields (u_a, v_a, and w_a). Figure 2c shows the distribution of the mean velocity component u_a on the equatorial plane ($z = 0$), whereas Figure 2d shows the distribution of u_a on the vertical plane, including the turbine rotation axis.

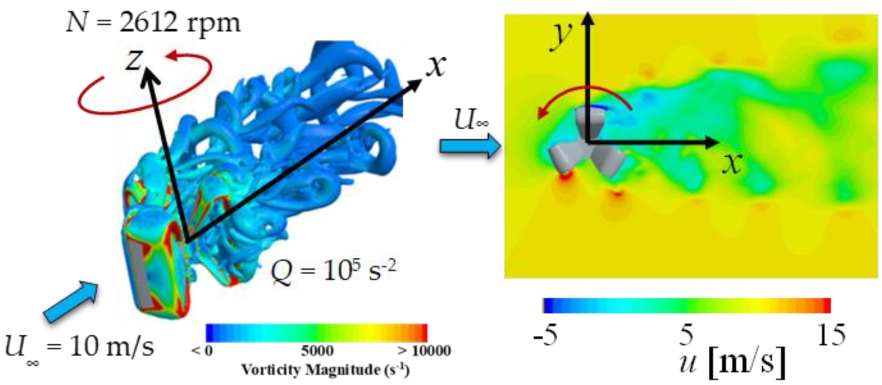

(**a**) Vortex shedding (**b**) Unsteady flow field

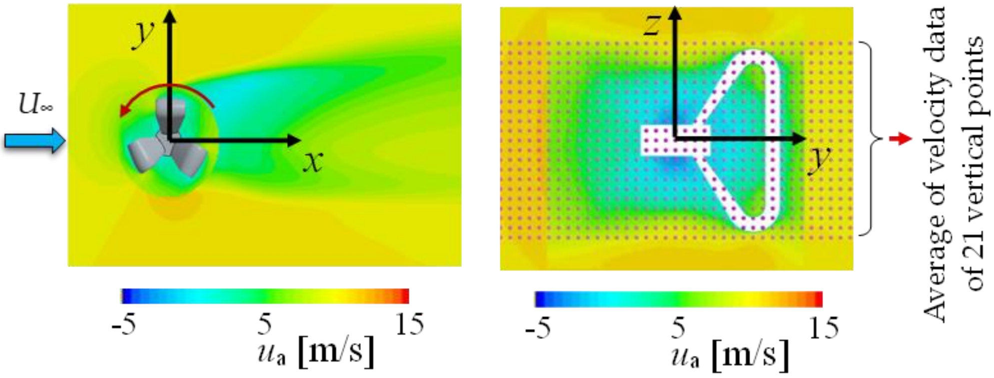

(**c**) Averaged flow field (over 10 rotations)

(**d**) Distribution of averaged flow speed in a vertical cross section

Figure 2. Unsteady flow field based on 3D-CFD simulation and averaged distributions of streamwise velocity component.

In this study, 44 vertical cross-sections perpendicular to the main flow direction were selected within the range x/D = -4 to 10 (e.g., $x/D = -4, -3, -2, -1, -0.75, -0.7, -0.6, \cdots, 0.6, 0.7, 0.75, 0.8, 0.9, \cdots, 2.4, 2.5, 3.0, 4.0, 6.0, 8.0, 10.0$). For each section, mean flow data (u_a, v_a, and w_a) were extracted within the region encompassed by $y/D = -8$ to 8 (interval 0.05, 321 points) and $z/D = -0.5$ to 0.5 (interval 0.05, 21 points). The red dots in Figure 2d indicate the sampling locations. By averaging the extracted data over 21 points in the z-direction, the mean flow data (u_a and v_a) (note that w_a was not used) were compressed in the vertical direction at each of the 44 cross-sections near the turbine. The resulting 2D compressed dataset (44 × 321 points) was used as the input for the VAWTWF software, which predicted the flow field and operating state of each rotor in a VAWT wind farm based on the IFCM.

During the execution of the IFCM, the compressed data at the 44 cross-sections were interpolated and extrapolated in the streamwise (x) and lateral (y) directions to generate a condensed 2D mean flow field (u_c and v_c) around a single turbine, which was then used for flow-field construction.

Although the v_c component was calculated within the VAWTWF, it was not used in this study to predict the turbine operating state. Furthermore, because the average velocity data u_a obtained inside the rotating region from the CFD analysis represent the values in a rotating reference frame (see Figures 2c and 2d), the compressed velocity data inside the rotating region were generated via linear interpolation using the condensed 2D data obtained in the surrounding stationary region 2 near the rotating-region boundary.

Figure 3a shows the distribution of the condensed 2D velocity component u_c near the rotor obtained using the procedure described above. Figure 3b shows a comparison of the distribution of u_c along the four dashed lines shown in Figure 3a ($x/D = -2$, 1, 2, and 4), with the streamwise velocity component u measured at the equatorial plane of the isolated experimental turbine using an I-type hot-wire probe (H.W.). As the turbine wake is a 3D flow with complex velocity distributions, the two profiles are naturally different. Nevertheless, a similarity was observed between the maximum velocity deficit and its lateral (y) position.

The core of the proposed method is to condense 3D-velocity data into 2D data. In this process, information on the vertical velocity component and the vertical distributions of the horizontal velocity components (i.e., the streamwise and secondary-flow components) is lost. However, the horizontal distributions of the vertically averaged horizontal velocity components (streamwise and secondary-flow components) are preserved. Figure 3b illustrates part of the retained information.

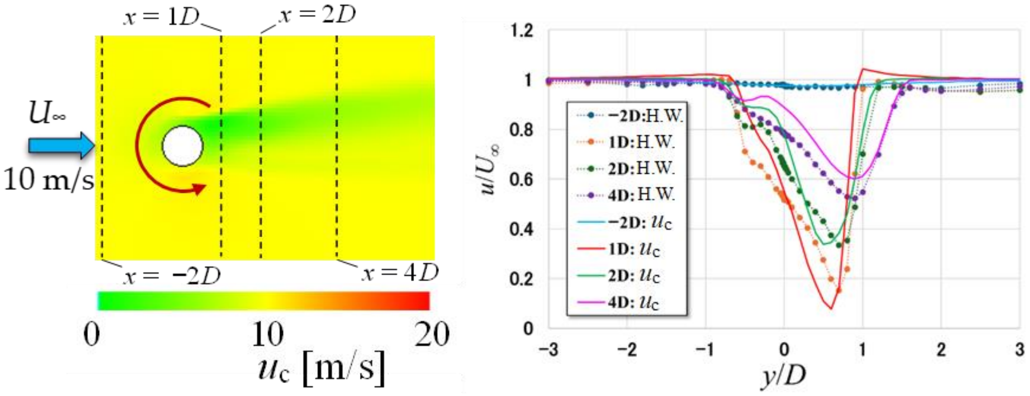

(**a**) Condensed 2D flow (**b**) Comparison of wake

Figure 3. Condensed 2D flow field around single VAWT and comparison with wake velocity measured using hot-wire probe.

2.2. Turbine Characteristics and Applied Load Torque

Under the inflow condition $U_\infty = 10$ m/s, 3D-CFD simulations of the isolated turbine described in the previous section were performed for rotational speeds ranging from 1000 to 4000 rpm at intervals of 500 rpm. The resulting shaft power P [mW] is plotted using circular red symbols, as shown in Figure 4. Additionally, the shaft power obtained from the 3D-CFD analysis at $N = 2612$ rpm described in Section 2.1 ($P = 128.7$ mW) is shown in Figure 4. The circular blue symbols in the figure represent the shaft powers measured in previous wind-tunnel experiments [26]. Although a slight discrepancy appeared near the maximum output, the CFD predictions agreed well with experimental data.

The monotonically increasing curve presented as a dashed line represents the predicted shaft power based on the load–torque curve (Load-2), which was inferred from the measured performance of the model turbine in the wind-tunnel experiment (2612 rpm, 93.1 mW at 10 m/s). Figure 5 shows the torque-rotation speed characteristics of the model turbine at wind speeds $U_\infty = 8$, 9, 10, 11, and 12 m/s. In the wind-tunnel experiments, the load torque was adjusted for each test (by varying the output resistance of the small motor used as a generator) to mitigate the effects of turbine-to-turbine performance variation. The three load–torque curves used in the measurements (Load-1 to Load-3) are shown in Figure 5. However, in the experiments described in Section 3, two load torques were applied: Load-1 and Load-3. Figure 6 presents the relationships between the inflow velocity U_∞ and rotational speed N, and between U_∞ and shaft power P, as determined from the intersection points of each load–torque curve with the turbine torque characteristics shown in Figure 5. As shown in Figure 5, the aerodynamic torque of the model turbine at 8 m/s is smaller than that shown in any of the load–torque curves. Consequently, as shown in Figure 6, the turbine does not rotate at wind speeds of 8 m/s or lower.

The experiments were conducted in an open space downstream of the wind-tunnel exit, where either a single or three turbines were installed under uniform, steady inflow conditions. As in the CFD model, the diameter D and height H of the experimental wind turbine were 50 mm and 43.4 mm, respectively, resulting in a swept area of 2.17×10^{-3} m^2. When three turbines were arranged in parallel, the maximum total swept area was 6.51×10^{-3} m^2, and the corresponding maximum blockage ratio relative to the wind tunnel cross-section (width 0.60 m × height 0.35 m) was only 3.1%. This value is significantly lower than the acceptable limit of 14%, below which blockage effects can be neglected for vertical-axis wind turbines installed in open wind tunnels, as reported in Ref. [33]. Therefore, no blockage correction was applied in this study. This is consistent with the approach of Ahmadi-Baloutaki et al. [34], who did not apply blockage correction in their wind-tunnel experiments on a wind-turbine trio (blockage ratio: 4.1%).

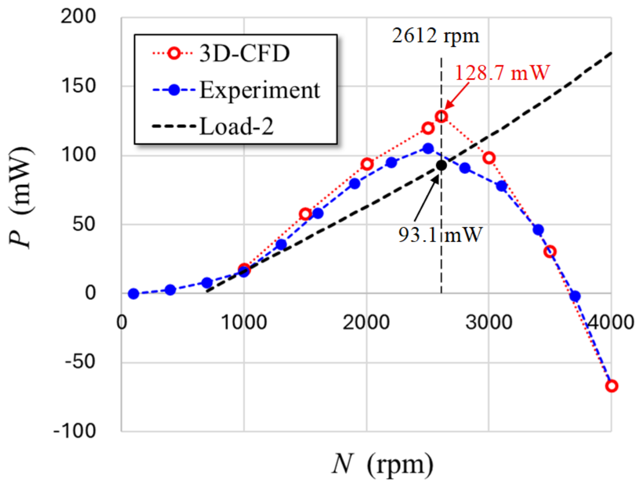

Figure 4. Shaft-power performance obtained via 3D-CFD simulations and wind-tunnel experiments under U_∞ = 10 m/s. Dotted curve represents load performance assumed for previous experimental VAWT with D = 50 mm.

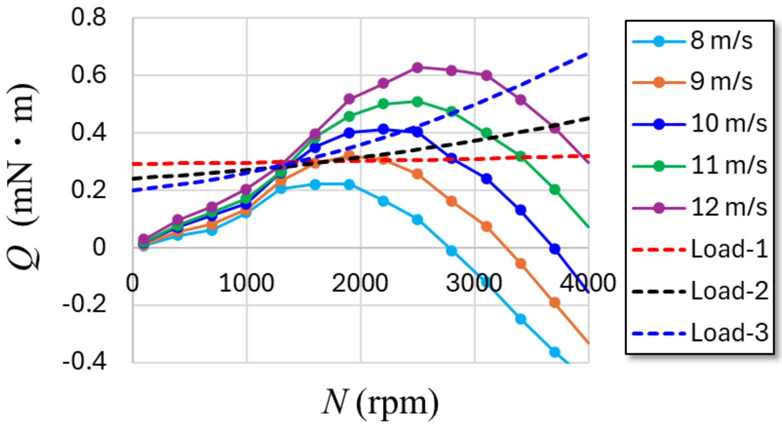

Figure 5. Torque performance obtained via wind-tunnel experiments at U_∞ = 8, 9, 10, 11, and 12 m/s and three load curves estimated for experimental VAWTs.

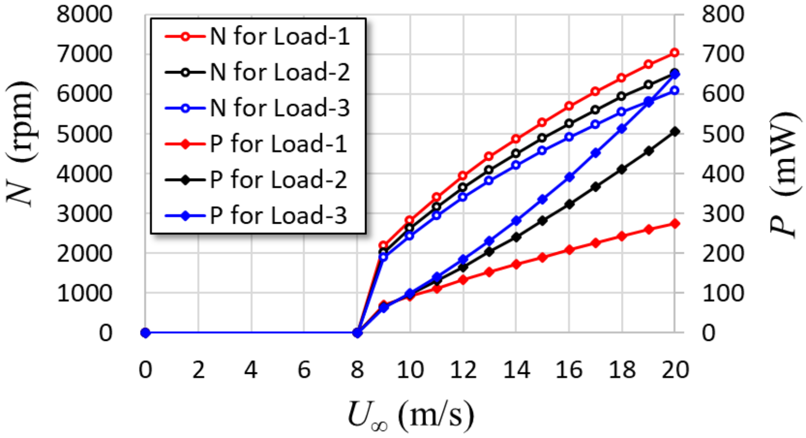

Figure 6. Conversion of upstream wind speed to turbine speed and shaft power for three load characteristics of miniature VAWT.

2.3. Fast Computational Method for VAWT Wind Farms

In this study, compressed 2D velocity data obtained from the 3D-CFD analysis were used as input to the in-house VAWTWF software, which is based on a previously developed IFCM for predicting the flow field in a VAWT wind farm [24]. A schematic representation of this method is shown in Figure 7. The condensed 2D velocity distributions (u_c and v_c) near the rotor, which were obtained by interpolating the input data, are illustrated on the right side of Figure 7. As mentioned earlier, the lateral velocity component v_c was calculated using the VAWTWF software, but was not used in the present turbine-operating state prediction. The difference between the present condensed velocity distribution and the 2D velocity field around a single turbine, as shown in Figure 2 of Ref. [24], where 2D-CFD data were used as the input, is noteworthy.

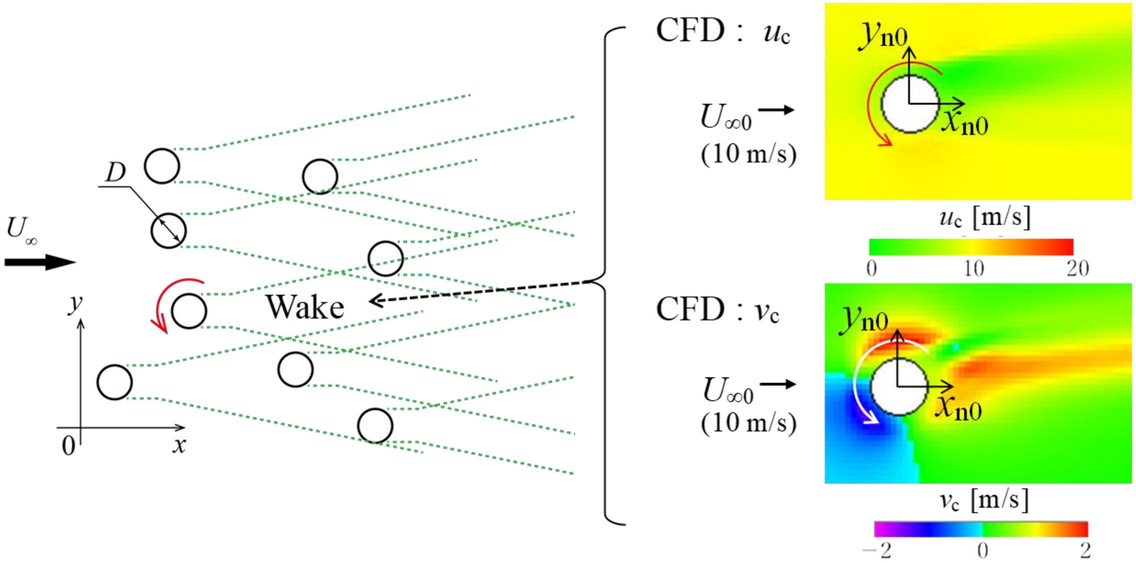

Figure 7. Conceptual image of flow-field construction of VAWT wind farm using condensed 2D velocity components (u_c and v_c) around isolated single VAWT.

In the proposed method, the normalized velocity difference du_{dif} between the condensed velocity u_c and the uniform upstream velocity $U_{\infty 0}$ assumed in the 3D-CFD simulation (in this study $U_{\infty 0} = U_\infty$ = 10 m/s) is calculated as follows:

$$du_{\mathrm{dif}}(x_{\mathrm{n0}},\ y_{\mathrm{n0}}) = \frac{1}{U_{\infty 0}}\{u_{\mathrm{c}}(x_{\mathrm{n0}},\ y_{\mathrm{n0}}) - U_{\infty 0}\} \tag{1}$$

Here, $(x_{\mathrm{n0}}, y_{\mathrm{n0}})$ are the coordinates normalized by the VAWT diameter D, with the center of the isolated single turbine regarded as the origin. The relative normalized coordinates, with the center (x_j, y_j) of the j-th VAWT in the wind farm as the origin, are specified in Equations (2) and (3).

$$x_n(j) = \frac{x - x_j}{D} \tag{2}$$

$$y_n(j) = \frac{y - y_j}{D} \tag{3}$$

Using the same procedure as Part 1 of method-2 shown in the flowchart of Figure 5 in Ref. [19], the streamwise velocity component u at an arbitrary location (x, y) in the VAWT wind farm was constructed using Equation (4) by increasing the temporary number of turbines N_{temp} sequentially from one to $(N - 1)$. In the superposition process in Equation (4), the streamwise velocity component was set to zero when a negative value was obtained.

$$u(x, y) = U_{\infty} + \sum_{j=1}^{N_{\mathrm{temp}}} U_{\mathrm{F}}(j)\, du_{\mathrm{dif}}(x_{\mathrm{n}}(j), y_{\mathrm{n}}(j)) \tag{4}$$

The present study differs from Ref. [24] in that the virtual upstream velocity of the j-th turbine, $U_{\mathrm{F}}(j)$, is expressed as shown in Equation (5).

$$U_{\mathrm{F}}(j) = u_{\mathrm{ave}}(j) \tag{5}$$

Additionally, correction terms $\Delta u1(j)$ or $\Delta u2(j)$, which were introduced previously, were not adopted in this study. In Equation (5), $u_{\mathrm{ave}}(j)$ denotes the average streamwise velocity evaluated at 11 equally spaced points along a line segment of length D perpendicular to the main flow and passing through the center of the j-th turbine, as shown in Figure 8. As described above, for simplicity, the virtual upstream velocity $U_{\mathrm{F}}(j)$ in this study is defined as the average of the streamwise velocity components along a straight line. Consequently, the influence of the velocity gradient on the operating conditions (i.e., rotational state) of the wind turbine is not considered. It should be noted that various approaches can be considered to obtain the representative velocity, such as averaging along the upstream semicircle of the rotor or using the velocity at a specific point without averaging. An appropriate definition of virtual upstream velocity remains an issue to be addressed in future studies.

Based on the Part 1 procedure using Equation (2), temporary values of the virtual upstream velocity $U_{\mathrm{F}}(j)$ were obtained for all the turbines in the VAWT wind farm. A flowchart of Part 1 is presented in Figure 9.

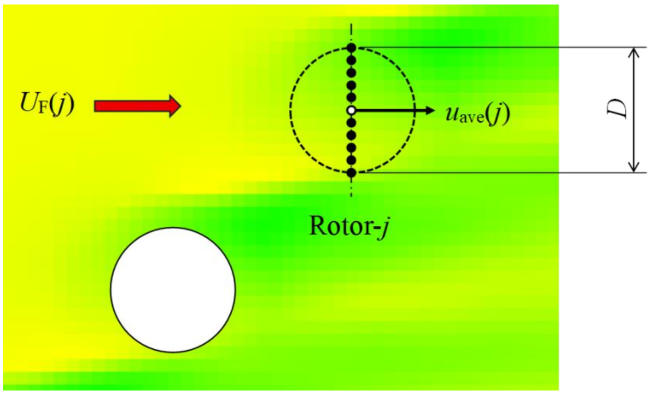

Figure 8. Range contributing to average streamwise velocity $u_{\mathrm{ave}}(j)$ at j-th wind turbine center, which is assumed as the virtual upstream wind speed U_{F}.

The subsequent computational process (Part 2) is identical to that shown in Figure 4 of Ref. [24]. One turbine (the q-th turbine) is removed sequentially from a total of N turbines, and the average velocity at the center of the removed turbine, $u_{\mathrm{ave}}(q)$—i.e., its virtual upstream velocity $U_{\mathrm{F}}(q)$—is recalculated using Equation (4) with $N_{\mathrm{temp}} = N - 1$. Once $U_{\mathrm{F}}(q)$ has been recalculated for all wind turbines, the updated flow field $u^{(RN)}$ is calculated using Equation (6) for the RN-th recalculation.

$$u^{(RN)}(x, y) = U_{\infty} + \sum_{j=1}^{N} U_{\mathrm{F}}^{(RN)}(j)\, du_{\mathrm{dif}}(x_{\mathrm{n}}(j),\ y_{\mathrm{n}}(j)) \tag{6}$$

The root-mean-square difference $winRMS$ between the virtual upstream velocities obtained in the RN-th and $(RN - 1)$-th iterations—$U_{\mathrm{F}}^{(RN)}(j)$ and $U_{\mathrm{F}}^{(RN-1)}(j)$, respectively—is evaluated using Equation (7).

$$winRMS = \sqrt{\frac{\sum_{j=1}^{N}\left(U_{\mathrm{F}}^{(RN)}(j) - U_{\mathrm{F}}^{(RN-1)}(j)\right)^{2}}{N}} \tag{7}$$

The iterative calculation is repeated until $winRMS$ becomes smaller than a prescribed tolerance ε. In this study, $\varepsilon = 0.0001$. The flowchart of Part 2 is shown in Figure 10. Once the Part 2 iterations converge, the converged virtual upstream velocity $U_{\mathrm{F}}(j)$ is regarded as the effective inflow velocity U_{∞} for each turbine, and the corresponding rotational speed N and shaft power P are determined based on Figure 6.

Figure 11 presents the computational workflow, beginning with the 3D-CFD analysis of a single turbine (S.T.) to estimate the rotational speed N and output power P for each wind turbine in the wind farm.

At present, the 3D-CFD simulation for a single isolated turbine is performed on a computer equipped with a 64-core CPU (3.2–5.1 GHz), requiring approximately 24 h to compute one rotor revolution. At least five revolutions are required for the flow field to converge. Therefore, when considering a cluster of three turbines, the minimum required computational time is estimated as $3600 \times 24 \times 5 \times 3 = 1.296 \times 10^{6}$ s. In contrast, the computational time required by the proposed method under the same conditions does not exceed 0.3 s, even when conservatively estimated. Thus, if the computational cost of CFD is considered 100%, the cost of the proposed method is estimated to be less than 2.3×10^{-5} %. Although the accuracy may be reduced to a certain extent, the extremely low computational cost makes the proposed approach highly suitable as an efficient engineering tool for wind farm design.

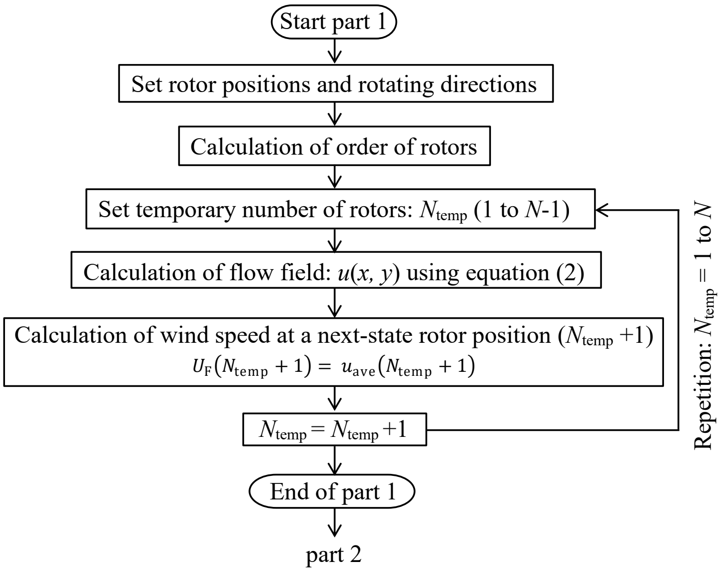

Figure 9. Flowchart of Part 1 of proposed method.

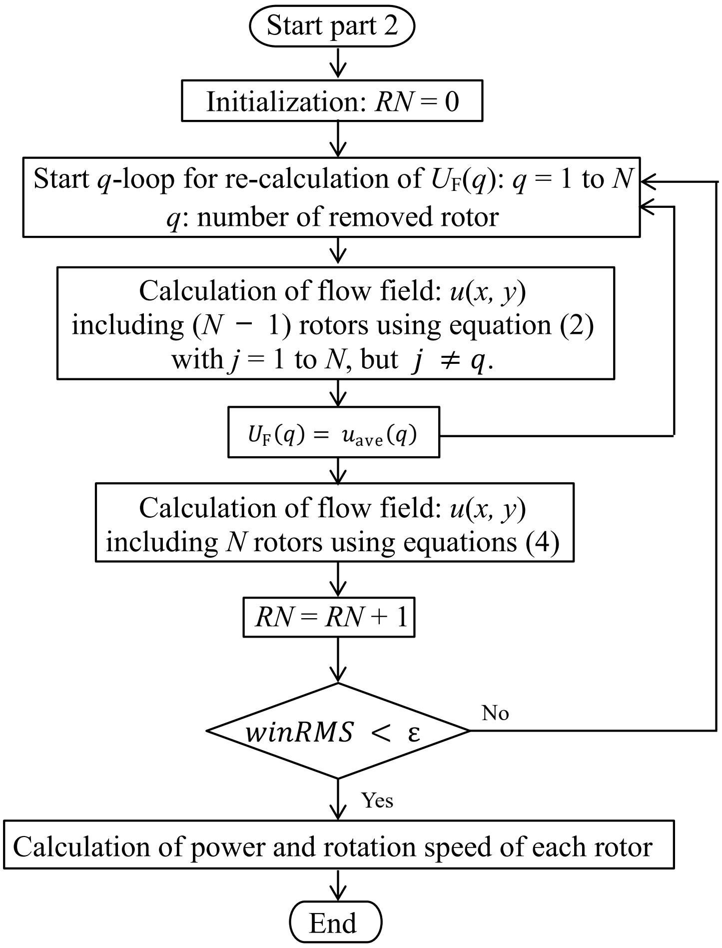

Figure 10. Flowchart of Part 2 of proposed method.

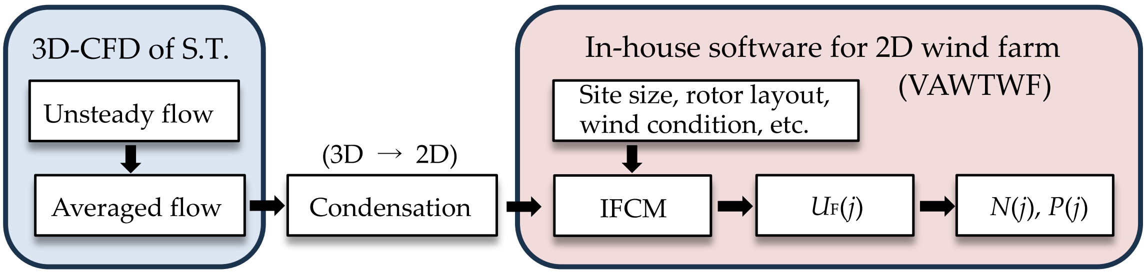

Figure 11. Work flow of the calculation of 2D wind farm of VAWTs.

3. Results and Discussion

3.1. Three Turbines Arranged in Parallel

The proposed method was applied to a VAWT cluster comprising three miniature turbines arranged in parallel and aligned perpendicularly to the incoming flow, as shown in Figure 12. In Figure 12, the black and white circles denote the VAWTs rotating clockwise (CW) and counterclockwise (CCW), respectively. The three turbines were equally spaced, and the spacing g was varied from 0.2D (10 mm) to 3D (150 mm). The inflow entered from the left, and the turbines were labeled from top to bottom as R1, R2, and R3. Four layout configurations were considered based on the rotation direction as follows: Cases 1 to 4 corresponding to (000), (100), (010), and (001), respectively, with "0" and "1" representing CW and CCW, respectively. In the wind-tunnel experiments [27], the freestream velocity was set to U_∞ = 12 m/s; therefore, U_∞ = 12 m/s was used in the predictive equations for the flow field $u(x, y)$, i.e., Equations (4) and (6). However, $U_{\infty 0}$ was set to 10 m/s. The origin of the coordinate system (x, y) in this study was set at the center of the VAWT cluster (center of R2 in Figure 12).

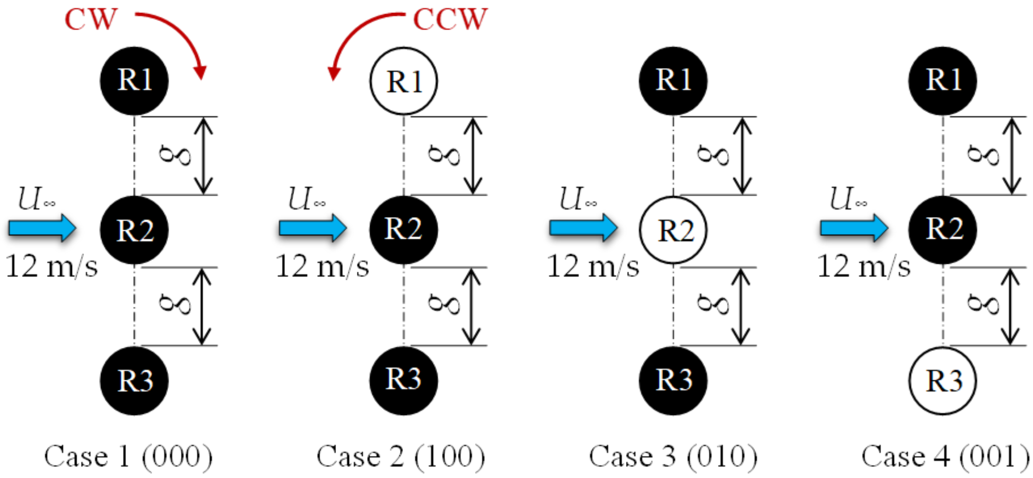

Figure 12. Four cases of three-rotor parallel arrangements.

Figure 13 shows the predicted flow fields (distributions of u) for the four cases at a turbine spacing of g = 0.5D (25 mm). Although the lateral component of the condensed velocity (the secondary-flow component) v_c was not considered when calculating the streamwise velocity component u, the wake deflection with respect to the rotation direction was captured, and the wake overlap (interference) was predicted in Cases 3 and 4. The predicted rotational speeds of each turbine are shown in Figure 13. For example, in Case 1, the predicted rotational speed decreased from R1 to R3, which is consistent with the expectations based on the induced velocity generated by the turbine rotation.

Figure 14 shows a comparison of the dependence of the rotational speed of each turbine on the inter-turbine spacing between the wind-tunnel measurements and predictions. Because the experimental data shown in Figure 14 were obtained under the Load-1 torque condition, the same load condition was assumed in the predictions. In Figure 14, the circular and square symbols represent the experimental data and predicted results, respectively. The blue and light-blue symbols correspond to R1; red and orange symbols correspond to R2; and white and black symbols correspond to R3. In general, the rotational speeds exhibited the following trends: in Case 1, R1 > R2 > R3; in Case 2, R2 > R1 > R3; in Case 3, R3 > R1 > R2; and in Case 4, R1 > R3 > R2. These relative relationships were reflected in both experiments and predictions. In the predictions, several cases exhibited a significant decrease or increase in the rotational speed at a minimum spacing g of 0.2D (10 mm), as compared with the case of g = 0.3D (15 mm). In general, for all layouts, as the spacing increased and approached g = 3D (150 mm), the rotational speed asymptotically approached that of a single isolated turbine (3931 rpm at U_∞ = 12 m/s and Load-1 (see Figure 6)). By contrast, the experimental results converged toward a constant value as the spacing increased; however, the asymptotic value differed depending on the turbine and layout. This difference is presumed to arise from individual variations among the model turbines.

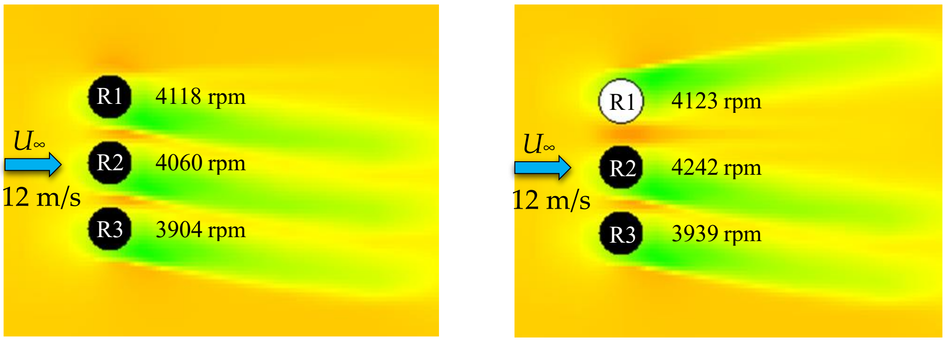

(**a**) Case 1 (**b**) Case 2

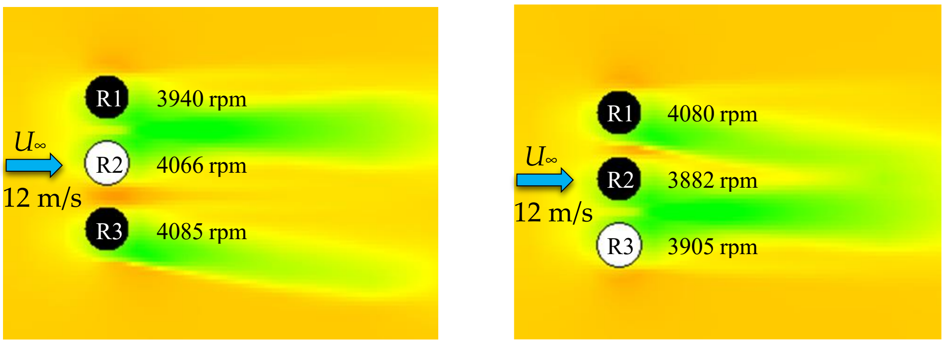

(**c**) Case 3 (**d**) Case 4

Figure 13. Predicted flow fields and rotational speeds for four cases with parallel arrangements and $g = 0.5D$ (25 mm).

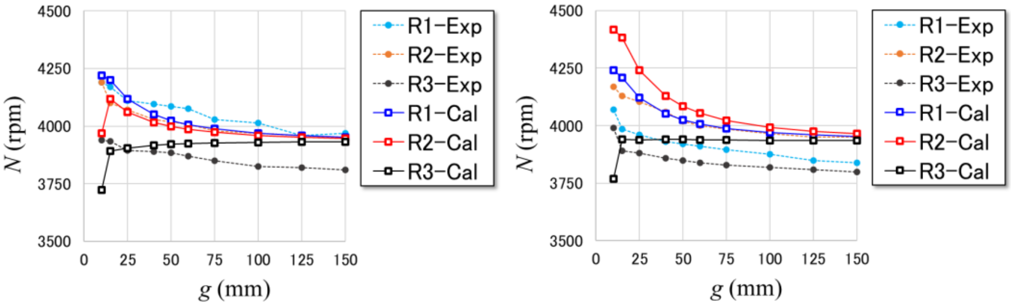

(**a**) Case 1 (000) (**b**) Case 2 (100)

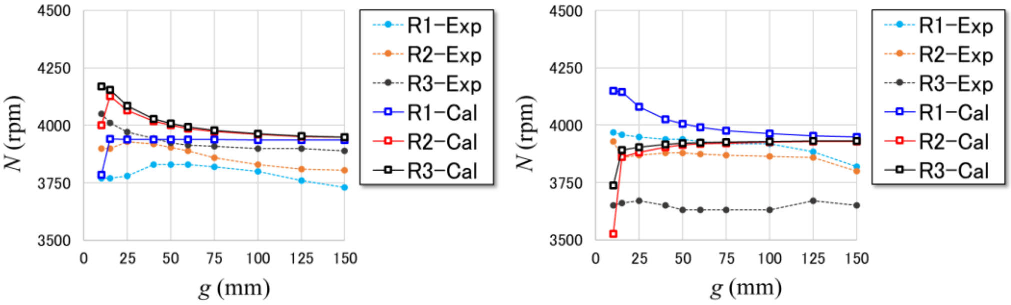

(**c**) Case 3 (010) (**d**) Case 4 (001)

Figure 14. Comparison of dependence of rotational speed of each turbine on inter-turbine spacing between wind-tunnel measurements and predictions for three-turbine parallel arrangements. In the experiments for Cases 1–4, the Load-1 torque condition was used.

In the wind tunnel experiments conducted in this study, the primary source of error arose from variations among individual wind turbines. Prior to each experiment, it was confirmed that, under isolated conditions at the same inflow velocity, the rotational speeds of the three turbines used fell within ±5% of their mean rotational speed. Therefore, the experimental uncertainty in this study was estimated to be ±5%.

In this study, using the predicted rotational speed N_{pred} as a reference, the error Err was expressed (see Equation (8)) as the absolute difference between the measured rotational speed in the wind-tunnel experiment N_{meas} and the predicted rotational speed divided by N_{pred}.

$$Err\ [\%] = \frac{\left|N_{\mathrm{pred}} - N_{\mathrm{meas}}\right|}{N_{\mathrm{pred}}} \times 100 \tag{8}$$

Tables 1 and 2 present comparisons of the errors predicted using the three methods, that is, Err predicted using the previously proposed triangular-wake model (TWM) [25] based on wake-velocity distributions measured using a hot-wire anemometer, which was predicted based on the 2D velocity field around a single rotor obtained from the 2D-CFD simulation, and that predicted based on the condensed 2D velocity field derived from the present 3D-CFD analysis. Each table presents the average error for the three wind turbines in each case (Ave.), the overall average error across all turbines in the four cases (Total Ave.), the standard deviation (σ), and the maximum error (Max. Err).

Table 1 presents the comparison based on g = 3D (150 mm). The proposed method yielded the smallest average error among all the prediction methods (2.87%). Table 2 presents a comparison based on g = 0.3D (15 mm). Although previous prediction methods exhibited maximum errors exceeding 23%, the proposed method limited the maximum error to less than 6%, thereby demonstrating a substantial improvement in prediction accuracy.

Table 1. Error comparison of three methods using different single turbine data based on g = 3D (150 mm).

S.T. data	**TWM based on H.W. meas. [25]**				**2D-CFD data [25]**				**3D-CFD data (present)**			
Case	**R1**	**R2**	**R3**	**Ave.**	**R1**	**R2**	**R3**	**Ave.**	**R1**	**R2**	**R3**	**Ave.**
Case 1	5.67	9.00	4.53	6.40	2.14	1.35	0.42	1.30	0.43	0.05	3.10	1.19
Case 2	2.15	5.45	4.34	3.98	6.30	5.62	2.86	4.92	2.86	0.38	3.46	2.23
Case 3	1.17	3.62	3.48	2.76	4.29	5.56	2.99	4.28	5.23	3.62	1.52	3.46
Case 4	1.68	7.25	1.06	3.33	3.92	1.20	4.40	3.17	3.29	3.31	7.17	4.59
Total Ave.	4.12				3.42				2.87			
σ	2.35				1.83				1.99			
Max. ***Err***	9.00				6.3				7.17			

Table 2. Error comparison of three methods using different single turbine data based on g = 0.3D (15 mm).

S.T. data	**TWM based on H.W. meas. [25]**				**2D-CFD data [25]**				**3D-CFD data (present)**			
Case	**R1**	**R2**	**R3**	**Ave.**	**R1**	**R2**	**R3**	**Ave.**	**R1**	**R2**	**R3**	**Ave.**

Case 1	19.28	23.38	18.10	20.25	11.11	10.46	4.00	8.52	0.71	0.41	1.10	0.74
Case 2	9.12	16.83	11.17	12.37	23.38	22.57	12.82	19.59	5.34	5.75	1.29	4.13
Case 3	1.86	6.09	14.97	7.64	10.77	19.72	17.18	15.89	4.36	5.52	3.49	4.46
Case 4	18.56	11.30	3.59	11.15	10.22	6.15	7.13	7.84	4.46	0.05	5.99	3.50
Total Ave.	12.86				12.96				3.21			
σ	6.48				6.10				2.22			
Max. ***Err***	23.38				23.38				5.99			

3.2. Three-Turbine Tandem Arrangement

Wind-tunnel experiments were conducted at the National Institute of Technology, Kagawa College, in which three miniature wind-turbine models were aligned in a straight line, and the relative position of the middle turbine varied [28]. Figure 15 shows the four independent layouts used in the experiments corresponding to tandem arrangements, where the main flow direction and turbine row are aligned parallel to each other. The freestream velocity is U_∞ = 12 m/s, and in Figure 15, the flow is assumed to proceed from left to right. The turbines are labeled R1, R2, and R3 from the upstream side. The experiments were performed with the center-to-center distance between R1 and R3 fixed at 8D (400 mm), while the spacing between R1 and R2 (g_1) and between R2 and R3 (g_2) varied. Because the relation $g_2 = 6D - g_1$ is valid, each configuration can be parameterized solely by g_1. The four layouts shown in Figure 15 are classified based on the rotation directions of R1 to R3 (CW: 0, CCW: 1), as follows: Case 1 (000), Case 2 (001), Case 3 (010), and Case 4 (011).

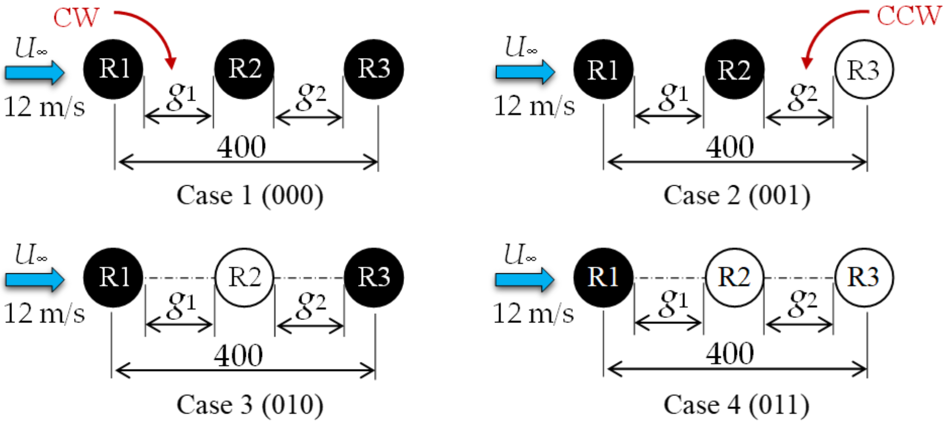

Figure 15. Four cases of three-rotor tandem arrangements.

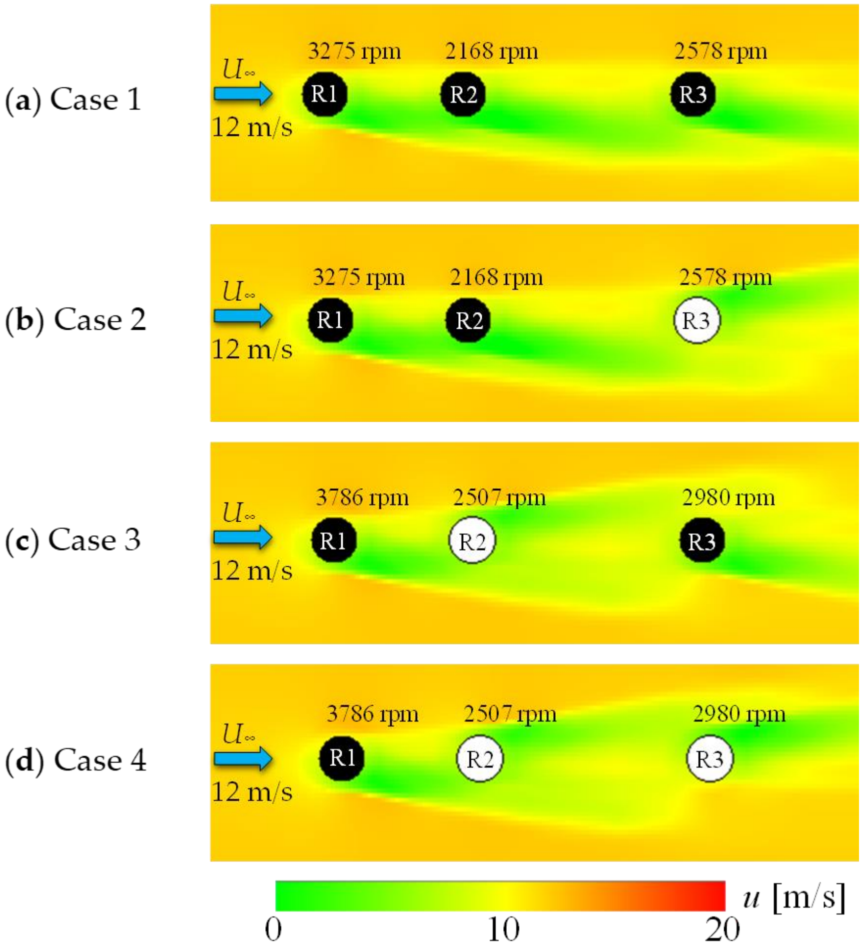

Figure 16. Predicted flow fields and rotational speeds for four cases with tandem arrangements and $g_1 = 2D$ (100 mm).

Figure 16 shows the flow fields and rotational speeds predicted for each turbine under $g_1 = 2D$ (100 mm) ($g_2 = 4D$ (200 mm)). The predicted rotational speeds were identical for Cases 1 and 2, and for Cases 3 and 4. This is because, in the present study, the virtual upstream wind speed U_F is defined based on Figure 8 as the average velocity component u_{ave} at 11 points within a distance equal to the rotor diameter. Consequently, the effect of the rotation direction cannot be captured even if a large velocity gradient exists. Although the accuracy might be improved by introducing previously proposed corrections [18] such as $\Delta u1$, which accounts for velocity gradients, or $\Delta u2$, which accounts for the secondary flow, this possibility shall be investigated in future studies.

Figure 17 shows a comparison of the wind-tunnel measurements with the predictions of the proposed method for the dependence of the turbine rotational speed on the inter-turbine spacing under the three-turbine tandem arrangement. In the wind-tunnel experiments (see Figure 17), Cases 1 and 2 were measured under a load torque of Load-3, whereas Cases 3 and 4 were measured under Load-1; therefore, the corresponding load torques were assumed in the predictions. The horizontal axis in Figure 17 represents turbine spacing g_1, and the remaining symbols are the same as those in Figure 14. As shown in Figure 16, the predicted rotational speeds were identical for Cases 1 and 2, and for Cases 3 and 4, regardless of g_1. In the experimental results for Cases 1 and 3, the rotational speed of the turbine farthest downstream, R3, became zero in some of the configurations. In particular, for Case 3 (Figure 17c), R3 halted when $g_1 \geqq 2D$ (100 mm); therefore, measurements were not conducted and the rotational-speed data for R1 and R2 are not reported.

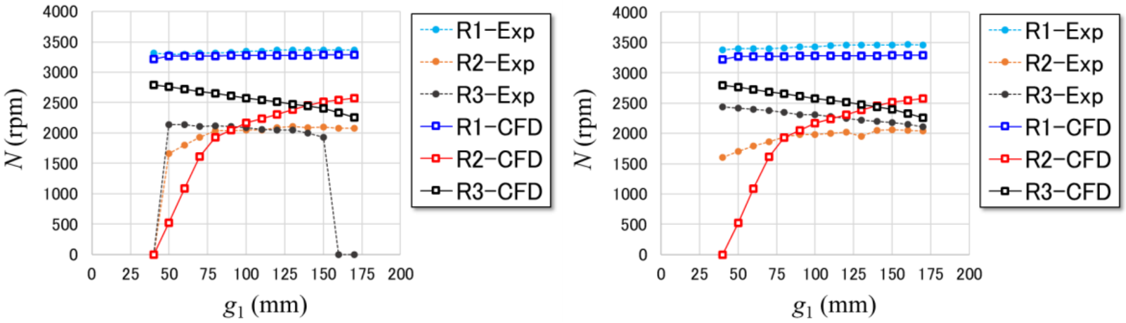

(**a**) Case 1 (000) (**b**) Case 2 (001)

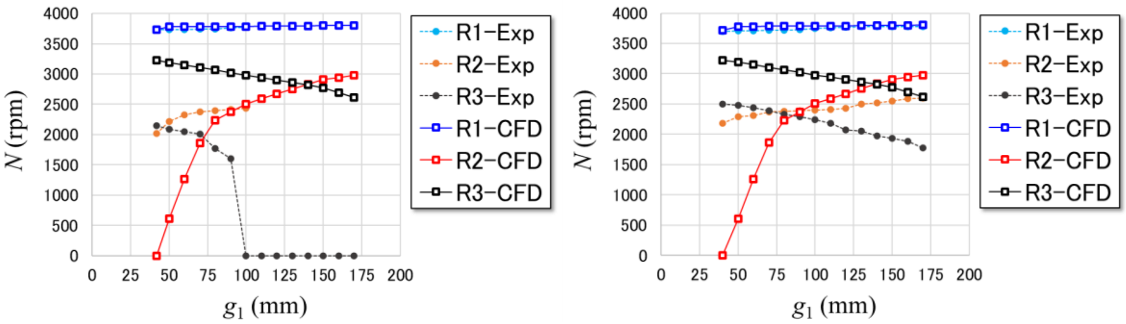

(**c**) Case 3 (010) (**d**) Case 4 (011)

Figure 17. Comparison of dependence of rotational speed of each turbine on inter-turbine spacing between wind-tunnel measurements and predictions under three-turbine tandem arrangements. In the experiments for Cases 1 and 2, the Load-3 torque condition was used, whereas in the experiments for Cases 3 and 4, the Load-1 torque condition was applied.

Table 3 shows a comparison of the prediction errors for g_1 = 1.8D (90 mm) and g_1 = 3.4D (170 mm). For g_1 = 1.8D (90 mm) (g_2 = 4.2D (210 mm)), the average errors of R1 and R2 were less than 2.2% in all cases, whereas the average error of R3 was much larger at 25.57%. For g_1 = 3.4D (170 mm) (g_2 = 2.6D (130 mm)), the average error of R1 remained below 2.8%, indicating good agreement. However, the average errors of R2 and R3 approached 20%, thus demonstrating the difficulty of predicting turbines located within the wake. Nevertheless, as shown in Figure 17, the proposed method qualitatively reproduced the experimental trends; the rotational speed of R2 increased with g_1, whereas that of R3 decreased monotonically.

Table 3. Error comparison between cases of g_1 =1.8D and 3.4D under three-turbine tandem arrangements.

g_1	**1.8D (90 mm)**			**3.4D (170 mm)**		
Case	**R1**	**R2**	**R3**	**R1**	**R2**	**R3**
Case 1	1.71	0.54	19.31	2.46	19.22	-
Case 2	4.76	3.46	11.66	5.20	20.78	6.72
Case 3	0.66	2.07	47.07	-	-	-
Case 4	1.59	0.80	24.25	0.60	12.66	31.93
Ave.	2.18	1.72	25.57	2.76	17.55	19.33
Total Ave.	9.82			12.45		
σ	13.54			10.13		

Max. *Err*	47.07	31.93

3.3. Trio-Turbine Arrangement

Figure 18 shows a trio-turbine configuration in which three miniature VAWTs are located at the vertices of an equilateral triangle. In this study, the turbines are numbered (R1, R2, and R3) as shown in Figure 18. In the left configuration, all three turbines rotate in the same direction (CCW rotation in Figure 18); this arrangement is referred to as 3CO. By contrast, in the right configuration, only R2 rotates in the CW direction, whereas R1 and R3 rotate in the CCW direction; this arrangement is referred to as 3IR. In the wind-tunnel experiments [29], the freestream velocity was $U_\infty = 12$ m/s. The relative wind direction angle θ between the incoming flow and trio arrangement is defined with respect to the direction perpendicular to the line segment connecting the centers of R1 and R2. In both the experiments and calculations, the freestream direction was fixed, and the turbine arrangement was rotated about its center in 30° increments, thereby yielding 12 relative wind directions. The spacings between any pair of turbines in the trio arrangement were identical, and the rotational speed of each turbine was measured for three spacings: $g = 0.5D$ (25 mm), $1D$ (50 mm), and $2D$ (100 mm).

Figure 19 presents the predicted flow field and rotational speeds obtained by applying the proposed method to the 3CO and 3IR arrangements for $g = 1D$ (50 mm) and $\theta = 30°$. In the wind-tunnel experiments of the trio turbines, the load torque corresponds to Load-3 (3400 rpm at $U_\infty = 12$ m/s, see Figure 6). Therefore, the predicted rotational speed N of the turbines, not in the wakes of other turbines such as R1 and R2 in Figure 19, is approximately 3400 rpm. In both arrangements, R3 rotated in the CCW direction, and the upstream turbine R1 rotated in the same direction. However, because the rotational direction of R2 differed between the two configurations, its effect caused the rotational speed of R3 in 3CO was higher than that in 3IR.

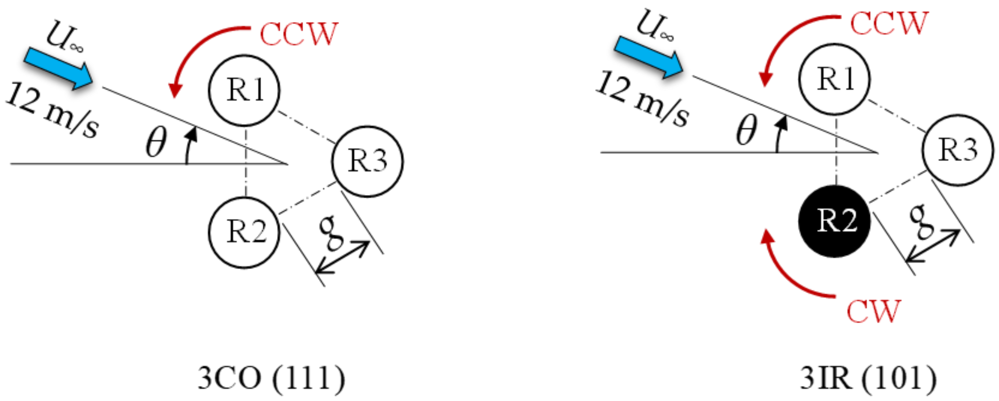

Figure 18. Two cases of trio arrangements and definition of relative inflow angle θ.

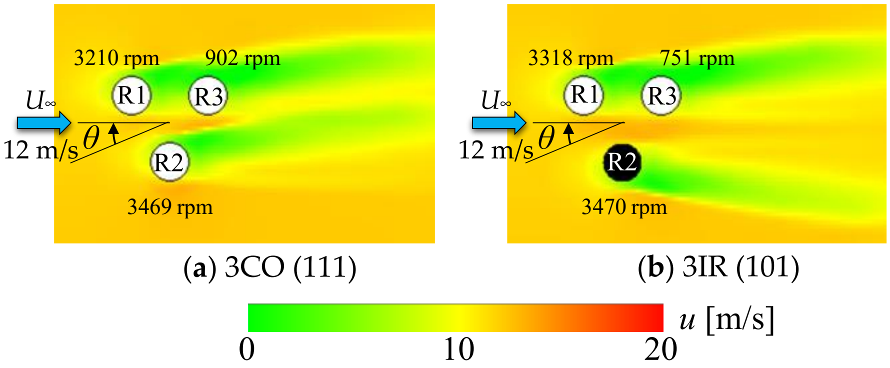

Figure 19. Predicted flow fields and rotational speeds for two cases with $g = 1D$ (50 mm) under trio arrangements.

Figures 20a and 20b present radar charts of the normalized rotational speed N_{norm} of each turbine for all relative wind directions in the 3CO configuration with g = 0.5D (25 mm), obtained experimentally and numerically, respectively. The normalized rotational speed is expressed using the isolated single-turbine rotational speed N_{SI} = 3400 rpm at U_∞ = 12 m/s by the following equation:

$$N_{\mathrm{norm}} = \frac{N}{N_{\mathrm{SI}}}. \tag{9}$$

The blue, green, and purple symbols indicate the normalized rotational speeds of R1, R2, and R3. The black symbols in Figure 20a (experiment) and red symbols in Figure 20b (calculation) represent the average normalized rotational speeds of the three turbines for each wind direction. Figure 20c compares the extracted average values.

Figures 20d, 20e, and 20f show the corresponding comparisons for the 3IR configuration at g = 0.5D (25 mm); the interpretation of the graphs is the same as that in Figures 20a–c. The minimum value of N_{norm} was zero, which corresponds to a stationary turbine. However, to avoid overlapping symbols, the radar-chart center was set to N_{norm} = −0.2. Figures 21a–f and 22a–f present the results for g = 1D (50 mm) and g = 2D (100 mm), respectively, with the same graphical interpretation as that shown in Figure 20.

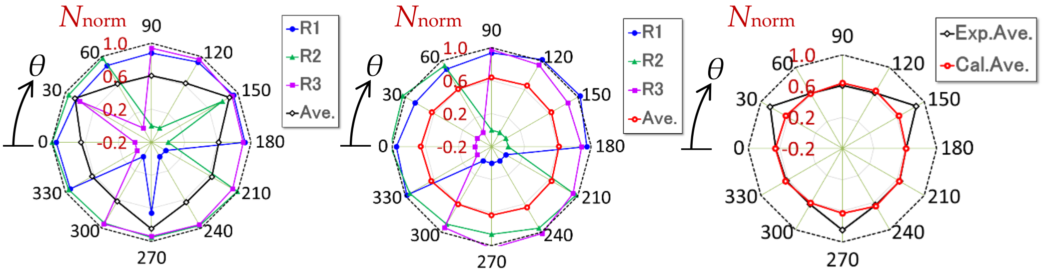

(**a**) 3CO: Exp. (**b**) 3CO: Cal. (**c**) 3CO: Ave.

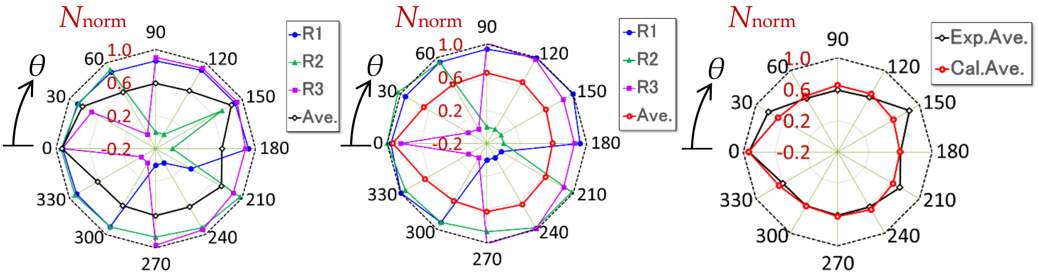

(**d**) 3IR: Exp. (**e**) 3IR: Cal. (**f**) 3IR: Ave.

Figure 20. Wind-direction dependence of normalized rotational speed N_{norm} of each turbine in trio configurations with g = 0.5D (25 mm): (**a**) experiments, (**b**) predictions , and (**c**) comparison of both in terms of three-rotor average, for 3CO case; (**d**) experiments, (**e**) predictions , and (**f**) comparison of both in terms of three-rotor average, for 3IR case.

Consider the case of θ = 30° in the 3CO configuration shown in Figures 20a and 20b. In the calculations, turbine R3 halts (N_{norm} = 0), whereas in the experiment, R3 shows N_{norm} = 0.794 (N = 2661 rpm), which distinguishes it from neighboring wind directions (θ = 0° and 60°, where N_{norm} = 0). Since the rotational speeds of R1 and R2 agreed well between the experiment and calculation at θ = 30°, a significant difference appeared in the averaged value shown in Figure 20c (by symmetry, the same occurred at θ = 150° and 270°). Except for this specific relative wind direction, the experimental and calculated average normalized rotational speeds of 3CO agreed well. Because 3IR is asymmetric (see Figure 20f), its distribution differed slightly from that of 3CO. However, although significant differences were observed in specific wind directions, the average values were almost identical for the other directions. In contrast, for g = 1D (50 mm), the average N_{norm} values shown in Figures 21c and 21f differed significantly between the experiment and calculation for many relative wind angles. This is presumed to be due to strong turbine–turbine interactions at a spacing comparable to the turbine diameter and the simplified definition of the virtual upstream velocity U_F using the average velocity u_{ave} in the present method. Improving the accuracy of this diameter-scale spacing region is a topic for future investigation. For g = 2D (100 mm), the averaged N_{norm} values in Figures 22c and 22f agreed well between the experiments and calculations, except for θ = 210° and 270° in 3IR.

Table 4 lists the errors for 3CO and 3IR over the 12 relative wind directions for g = 0.5D (25 mm), 1D (50 mm), and 2D (100 mm). As discussed above, when g = 1D the mean error averaged over the 12 directions was large: 20.07% for 3CO and 17.50% for 3IR. For g = 0.5D, however, the mean error decreased to approximately half of that value (10.84% for 3CO and 9.61% for 3IR). For g = 2D, the mean error further decreased to 3.97% for 3CO and 6.81% for 3IR.

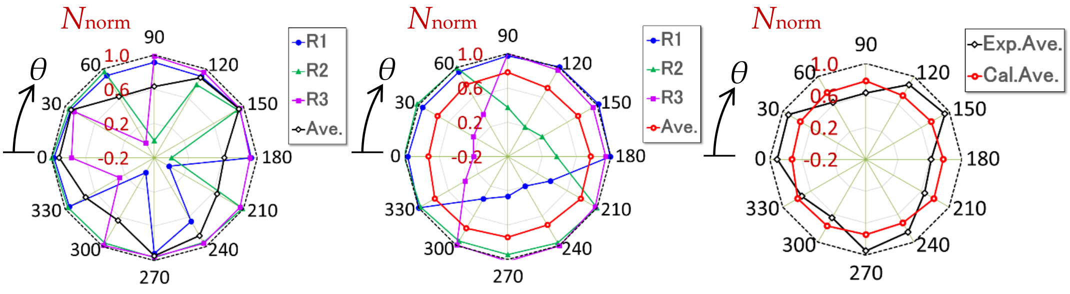

(**a**) 3CO: Exp. (**b**) 3CO: Cal. (**c**) 3CO: Ave.

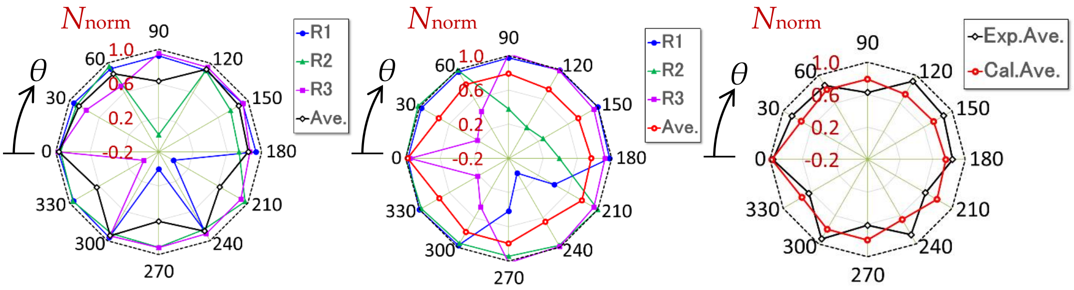

(**d**) 3IR: Exp. (**e**) 3IR: Cal. (**f**) 3IR: Ave.

Figure 21. Wind-direction dependence of normalized rotational speed N_{norm} of each turbine in trio configurations with g = 1D (50 mm): (**a**) experiments, (**b**) predictions , and (**c**) comparison of both in terms of three-rotor average, for 3CO case; (**d**) experiments, (**e**) predictions , and (**f**) comparison of both in terms of three-rotor average, for 3IR case.

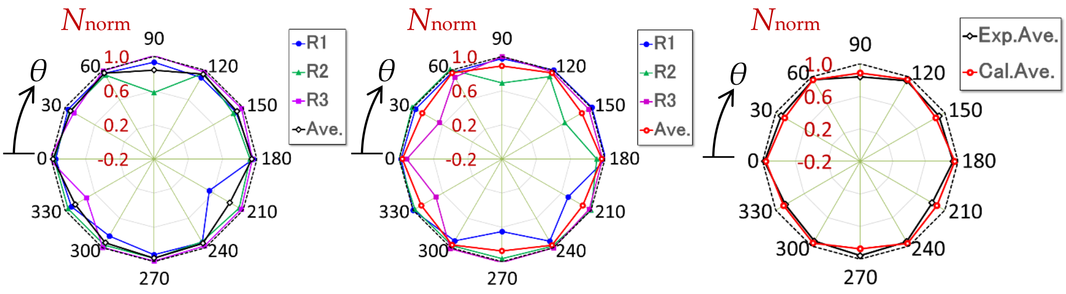

(**a**) 3CO: Exp. (**b**) 3CO: Cal. (**c**) 3CO: Ave.

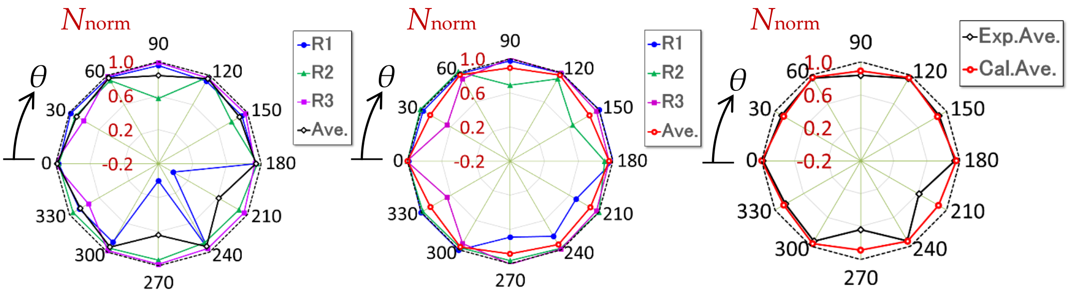

(**d**) 3IR: Exp. (**e**) 3IR: Cal. (**f**) 3IR: Ave.

Figure 22. Wind-direction dependence of normalized rotational speed N_{norm} of each turbine in trio configurations with g = 2D (100 mm): (**a**) experiments, (**b**) predictions , and (**c**) comparison of both in terms of three-rotor average, for 3CO case; (**d**) experiments, (**e**) predictions , and (**f**) comparison of both in terms of three-rotor average, for 3IR case.

Table 4. Error comparison among the cases of g = 0.5D, 1D, and 2D in trio arrangements.

g	**0.5*D* (25 mm)**		**1*D* (50 mm)**		**2*D* (100 mm)**	
Angle: *θ*[°]	**3CO**	**3IR**	**3CO**	**3IR**	**3CO**	**3IR**
0	0.98	0.36	25.66	1.44	1.53	1.53
30	36.75	20.76	23.40	17.98	5.62	2.77
60	1.42	5.14	18.68	6.94	0.17	0.77
90	4.85	9.47	19.13	20.95	5.44	6.12
120	4.38	7.26	21.58	25.14	1.92	0.96
150	39.80	37.54	26.39	19.22	5.01	2.71
180	0.03	1.12	19.79	10.57	2.09	1.70
210	0.56	16.00	17.48	20.86	7.63	30.69
240	2.31	6.09	17.86	32.94	2.45	0.51
270	34.05	2.22	27.49	22.84	9.71	27.98
300	3.10	0.90	15.84	17.54	3.03	3.29
330	1.84	8.41	7.57	13.54	3.04	2.73
Ave.	10.84	9.61	20.07	17.50	3.97	6.81
σ	15.13	10.30	5.23	8.09	2.65	10.19

Max. ***Err***	39.80	37.54	27.49	32.94	9.71	30.69

4. Conclusions

In this study, to render the previously developed fast computation method (IFCM) for predicting the flow field and turbine-operating state in VAWT wind farms applicable to actual turbines, a procedure was proposed in which a compressed 2D velocity dataset was generated from the 3D-CFD analysis of a target turbine and subsequently used to construct the flow field of a VAWT wind farm. The proposed method was applied to three types of turbine clusters, each comprising three miniature turbines with a diameter of 50 mm (parallel, tandem, and trio arrangements) that had been tested previously, and the predicted rotational speeds were compared with the experimental measurements. The main findings are summarized as follows.

✓ **Parallel arrangement (three turbines):**

The prediction accuracy obtained using the condensed 2D velocity data derived from the 3D-CFD simulation was significantly better than that of previous approaches adopting the TWM, which mimics wake-velocity distributions measured by a hot-wire anemometer, and that of predictions based on 2D-CFD velocity fields.

✓ **Tandem arrangement (three turbines):**

In two different three-turbine tandem configurations, when the rotation directions of the first two turbines upstream (R1 and R2) were the same, and only the rotation direction of the third turbine (R3) was different, the proposed method predicted the same rotation speed for both corresponding turbines. This is because the virtual upstream wind speed U_F was expressed as the average u_{ave} of the streamwise velocity on a line segment equivalent to the diameter of the VAWT. This result suggests that further improvement requires the incorporation of corrections that account for velocity gradients and/or secondary-flow effects.

✓ **Tandem arrangement—spacing effects:**

When the distance between the first and second turbines (R1–R2) was short (approximately 1.8D), the average errors for R1 and R2 in the four tandem arrangements were relatively small (less than 3%), whereas the average error for the third turbine (R3) exceeded 25%. Conversely, when the R1–R2 spacing was large (approximately 3.4D) and the R2–R3 spacing decreased, the average errors for R2 and R3 were approximately 20%.

✓ **Trio (equilateral-triangle) arrangement:**

When the turbine spacing was approximately equal to the rotor diameter, the average error over the 12 relative wind directions was approximately 20%. However, when the spacing was 2.0D, the average error decreased to 4%–7%, and further increases in spacing were expected to improve the accuracy.

The method using the condensed 2D velocity data proposed in this study could predict the experimental results with relatively good accuracy for parallel configurations, even when the turbine spacing was small. In contrast, for the tandem configurations, although the general trends were captured to some extent, the errors increased for the downstream turbines located in the wake. In the case of a wind-turbine trio, the errors increased when the turbine spacing was on the order of the rotor diameter. These results indicate that further improvements are necessary to incorporate the interference effects between turbines more accurately into the prediction method. Nevertheless, once a single 3D-CFD simulation of an isolated turbine is performed to generate a compressed 2D velocity field, subsequent analyses are essentially two-dimensional and thus computationally inexpensive. Therefore, the proposed method is expected to be useful for solving problems such as optimizing the layouts of VAWT wind farms.

The results demonstrate the validity of applying the proposed method to high-solidity-miniature VAWTs used in wind-tunnel experiments. Future studies should extend their applicability to full-scale VAWTs with lower solidities and verify their effectiveness. For full-scale VAWTs with low solidity, the turbine–turbine interaction effect is expected to reverse (see Figure 4 in [23]);

therefore, it is necessary to incorporate this effect into the virtual upstream wind velocity. Although performing 3D-CFD simulations becomes computationally demanding as the turbine size increases, the method and computational program proposed in this study can be applied without significant modification, provided that reliable 3D-CFD results are obtained under representative operating conditions. Although obtaining experimental data on turbine performance is expected to be difficult, approximate turbine characteristics can be derived using simplified models, such as blade element momentum theory, calibrated against a limited number of 3D-CFD results.

Author Contributions: Conceptualization, Y. H.; methodology, M. S. M. and Y.H.; software, Y. H.; validation, M. S. M., H.I. and Y. J.; formal analysis, Y. H. and M. S. M.; investigation, M. S. M., H.I. and Y. J.; resources, Y. H. and Y. J.; data curation, M. S. M., H.I. and Y. H.; writing—original draft preparation, M. S. M., H.I. and Y. H.; writing—review and editing, Y. J. and H. Z.; visualization, M. S. M. and Y.H.; supervision, Y. H.; project administration, Y. H.; funding acquisition, Y. H., Y. J., and H. Z. All authors have read and agreed to the published version of the manuscript.

Funding: This research was supported by the Iwatani Naoji Foundation, JSPS KAKENHI, grant number JP22K12456, and, in part, by the Collaborative Research Program of the Research Institute for Applied Mechanics, Kyushu University, project number 2025S3-CD-2.

Data Availability Statement: The data presented in this study are available upon request from the corresponding authors.

Acknowledgments: The authors used ChatGPT (OpenAI, GPT-4.1) to assist with translation from Japanese to English and to generate preliminary suggestions for relevant literature. The authors take full responsibility for the accuracy, integrity, and originality of the final manuscript.

Conflicts of Interest: The authors declare no conflicts of interest.

Abbreviations

The following abbreviations are used in this manuscript:

CCW	Counter clockwise
CFD	Computational fluid dynamics
CO	Co-rotation
CW	Clockwise
HAWT	Horizontal-axis wind turbine
H.W.	Hot-wire anemometer
IFCM	Improved fast computation method
IR	Inverse rotation
RMS	Root mean square
RN	Repetition number
S.T.	Single turbine
VAWT	Vertical-axis wind turbine
2D	Two dimensional
3D	Three dimensional

References

1. Mikindani, D.; Deeney, P.; Dunphy, N.P. Economic impacts of repowering wind turbines: A comparative analysis of advanced wind turbine technologies. *Sustain. Energy Res.* **2025**, *12*, 37. DOI:10.1186/s40807-025-00187-7.
2. Spiru, P.; Simona, P.L. Wind energy resource assessment and wind turbine selection analysis for sustainable energy production. *Sci. Rep.* **2024**, *14*, 10708. DOI:10.1038/s41598-024-61350-6.
3. Guan, J. Landscape visual impact evaluation for onshore wind farm: A case study. *ISPRS Int. J. Geo-Inf.* **2022**, *11*, 594. DOI:10.3390/ijgi11120594.

4. Teff-Seker, Y.; Berger-Tal, O.; Lehnardt, Y.; Teschner, N. Noise pollution from wind turbines and its effects on wildlife: A cross-national analysis of current policies and planning regulations. *Renew. Sustain. Energy Rev.* **2022**, *168*, 112801. DOI:10.1016/j.rser.2022.112801.
5. Didane, D.H.; Behery, M.R.; Al-Ghriybah, M.; Manshoor, B. Recent progress in design and performance analysis of vertical-axis wind turbines—A comprehensive review. *Processes* **2024**, *12*, 1094. DOI:10.3390/pr12061094.
6. Hezaveh, S. H.; Bou-Zeid, E.; Dabiri, J.; Kinzel, M.; Cortina, G.; Martinelli, L. Increasing the power production of vertical-axis wind-turbine farms using synergistic clustering. *Boundary-Layer Meteorol.* **2018**, *169*, 275–296. DOI:10.1007/s10546-018-0368-0.
7. Zhang, J.H.; Lien, F.S.; Yee, E. Investigations of vertical-axis wind-turbine group synergy using an actuator line model. *Energies* **2022**, *15*, 6211. DOI:10.3390/en15176211.
8. Sahebzadeh, S.; Rezaeiha, A.; Montazeri, H. Vertical-axis wind-turbine farm design: Impact of rotor setting and relative arrangement on aerodynamic performance of double rotor arrays. *Energy Rep.* **2022**, *8*, 5793–5819. DOI:10.1016/j.egyr.2022.04.030.
9. Bensason, D.; Mulay, J.; Sciacchitano, A.; Ferreira, C. Experimental demonstration of regenerative wind farming using a high-density layout of vertical-axis wind turbines. *Wind Energy Sci.* **2025**, *10*, 1499–1528. DOI:10.5194/wes-10-1499-2025.
10. Randall, R.; Chen, C.; Ageze, M.B.; Tigabu, M.T. Perspectives of vertical axis wind turbines in cluster configurations. *Fluid Dyn. Mater. Process.* **2024**, *20*, 2657–2691. DOI:10.32604/fdmp.2024.058169.
11. Dabiri, J. O. Potential order-of-magnitude enhancement of wind farm power density via counter-rotating vertical-axis wind turbine arrays. *J. Renew. Sustain. Energy* **2011**, *3*, 043104. DOI:10.1063/1.3608170.
12. Rolin, V. F.-C.; Porté-Agel, F. Experimental investigation of vertical-axis wind-turbine wakes in boundary layer flow. *Renew. Energy* **2018**, *118*, 1–13. DOI:10.1016/j.renene.2017.10.105.
13. Peng, H.Y.; Liu, H.J.; Yang, J.H. A review on the wake aerodynamics of H-rotor vertical axis wind turbines. *Energy* **2021**, *232*, 121003. DOI:10.1016/j.energy.2021.121003.
14. Elkhoury, M.; Kiwata, T.; Aoun, E. Experimental and numerical investigation of a three-dimensional vertical-axis wind turbine with variable-pitch. *J. Wind Eng. Ind. Aerodyn.* **2015**, *139*, 111–123. DOI:10.1016/j.jweia.2015.01.004.
15. Chen, X.; Agarwal, R. Optimal placement of horizontal- and vertical-axis wind turbines in a wind farm for maximum power generation using a genetic algorithm. *Int. J. Energy Environ.* **2012**, *3*, 927–938. DOI:10.1115/ES2011-54080.
16. Lam, H.F.; Peng, H.Y. Development of a wake model for Darrieus-type straight-bladed vertical axis wind turbines and its application to micro-siting problems. *Renew. Energy* **2017**, *114*, 830–842. DOI:10.1016/j.renene.2017.07.094.
17. Hansen, M.; Enevoldsen, P.; Abkar, M. Energy harvesting via co-locating horizontal- and vertical-axis wind turbines. *J. Phys.: Conf. S.* **2020**, *1618*, 032004. DOI:10.1088/1742-6596/1618/3/032004.
18. Bangga, G.; Dessoky, A.; Wu, Z.; Rogowski, K.; Hansen, M. O. L. Accuracy and consistency of CFD and engineering models for simulating vertical axis wind turbine loads. *Energy*, **2020**, 206, 118087, DOI:10.1016/j.energy.2020.118087.
19. Brusca, S.; Cucinotta, F.; Galvagno, A.; Sfravara, F.; Chillemi, M. Development of a numerical characterization method for a ducted Savonius turbine with power augmenters. *Energies*, **2025**, 18, 1142, DOI:10.3390/en18051142.
20. Chen, Y.; Zhang, D.; Li, X.; Peng, Y.; Zhang, X.; Han, Z.; Cao, Y.; Dong, Z. Surrogate models for twin-VAWT performance based on Kriging and artificial neural networks. *Ocean Eng*. **2023**, 273, 113947, DOI:10.1016/j.oceaneng.2023.113947.
21. Krige, D.G. A statistical approach to some basic mine valuation problems on the Witwatersrand. *J. S. Afr. Inst. Min. Metall*. **1951**, 52, 119–139. DOI:10.10520/AJA0038223X_4792.
22. Kingma, D. P.; Ba, J. L. Adam: a method for stochastic optimization. *Proceedings International Conference on Learning Representations (ICLR)*, **2015**, https://arxiv.org/abs/1412.6980v5.
23. Hara, Y.; Moral, M.S.; Ide, A.; Jodai, Y. Fast simulation of the flow field in a VAWT wind farm using the numerical data obtained by CFD analysis for a single rotor. *Energies* **2025**, *18*, 220. DOI:10.3390/en18010220.

24. Moral, M.S.; Hara, Y.; Jodai, Y. Improvement of fast simulation method of the flow field in vertical-axis wind turbine wind farms and consideration of the effects of turbine selection order. *Energies* **2025**, *18*, 6294. DOI:10.3390/en18236294.
25. Moral, M.S.; Inai, H.; Hara, Y.; Jodai, Y.; Zhu, H. Prediction of flow field and rotor performance of three-rotor parallel layout of experimental miniature vertical axis wind turbines by a fast computation method. In The Eleventh JSME–KSME Thermal and Fluids Engineering Conference (J-K TFEC11), Okinawa, Japan, 2025, 1428. https://repository.lib.tottori-u.ac.jp/record/2002084/files/JK-TFEC_1428.pdf
26. Jodai, Y.; Hara, Y. Wind tunnel experiments on interaction between two closely spaced vertical-axis wind turbines in side-by-side arrangement. *Energies* **2021**, *14*, 7874. DOI:10.3390/en14237874.
27. Jodai, Y.; Hara, Y.; Marusasa, K.; Mukai, K. Wind tunnel experiments on interaction among a trio of miniature vertical-axis wind turbines arranged in parallel. *The 46th Wind Energy Symposium*; **2024**, P-5. Available online:https://repository.lib.tottori-u.ac.jp/record/2002081/files/WES46th.pdf (accessed on 26 Feb. 2026).
28. Jodai, Y.; Hara, Y. Wind tunnel experiments on interaction between three vertical-axis wind turbines arranged in tandem. *J. Flow Control Meas. Vis.* **2019**, *7*, 75–88. DOI:10.4236/jfcmv.2019.73006.
29. Jodai, Y.; Hara, Y. Wind-tunnel experiments on the interactions among a pair/trio of closely spaced vertical-axis wind turbines. *Energies* **2023**, *16*, 1088. DOI:10.3390/en16031088.
30. Jodai, Y.; Tokuda, H.; Hara, Y. Experiments on interaction between six vertical-axis wind turbines in pairs or trios. *J. Phys.: Conf. S.* **2024**, *2767*, 072003. DOI:10.1088/1742-6596/2767/7/072003.
31. Menter, F. R. Two-equation eddy-viscosity turbulence models for engineering applications. *AIAA* **1994**, *32*, 1598–1605. DOI:10.2514/3.12149.
32. Kumari, S.; Tiwari, H.L.; Chavan, H. Advanced numerical investigation of flow Field and morphological evolution around tandem piers. *Environ. Fluid Mech.* **2022**, *22*, 1079–1103. DOI:10.1007/s10652-022-09866-3.
33. van Bussel, G. J. W.; Polinder, H.; Sidler, H. F. A. The development of *Turby*®, a small VAWT for the built environment, *Proceedings of the Global Windpower 2004 Conference & Exhibition, AWEA, Washington*, **2004**, 1-10. https://www.researchgate.net/publication/262643522_The_development_of_Turby_a_small_VAWT_for_the_built_environment.
34. Ahmadi-Baloutaki, M.; Carriveau, R.; Ting, D.S.-K. A wind tunnel study on the aerodynamic interaction of vertical axis wind turbines in array configurations. *Renew. Energy*, **2016**, 96, 904–913, DOI:10.1016/j.renene.2016.05.060.